

# Facile mechanochemical modification of g-C<sub>3</sub>N<sub>4</sub> for selective photo-oxidation of benzyl alcohol

Kenneth Cerdan<sup>a</sup>, Weiyi Ouyang<sup>a</sup>, Juan C. Colmenares<sup>b</sup>, Mario J. Muñoz-Batista<sup>a</sup>,

Rafael Luque<sup>a</sup>, Alina M. Balu<sup>a\*</sup>

<sup>a</sup>*Departamento de Química Orgánica, Universidad de Córdoba, Edificio Marie Curie (C-3), Ctra Nnal IV-A, Km 396, E14014, Córdoba, Spain. E-mail: [rafael.luque@uco.es](mailto:rafael.luque@uco.es)*

<sup>b</sup>*Institute of Physical Chemistry PAS, Kasprzaka 44/52, 01-224 Warsaw (Poland)*

## Abstract

Graphitic carbon nitride enriched with ZnO or Fe<sub>2</sub>O<sub>3</sub> were synthesized using a simple one-pot mechanochemical method. By using this method, composite samples were synthesized without the production of any potentially hazardous waste. The synthesized materials were used as catalysts during the selective photo-oxidation of benzyl alcohol. Both composite materials displayed an enhancement of the activity and benzaldehyde selectivity with respect to the pure g-C<sub>3</sub>N<sub>4</sub>. The most active catalyst was Fe<sub>2</sub>O<sub>3</sub>/g-C<sub>3</sub>N<sub>4</sub>. The conversion and benzaldehyde selectivity of this sample were 20 and 70 %, respectively. It showed a considerable increase of the benzaldehyde selectivity compared to the pure g-C<sub>3</sub>N<sub>4</sub> and TiO<sub>2</sub> P25 commercial reference. A complete structural and electronic characterization using Scanning Electron Microscopy-Energy Dispersive (SEM-EDX), BET measurements, X-ray diffraction (XRD), X-ray Photoelectron (XPS), and UV–visible spectroscopies was carried out. The characterization analysis pointed out the leading role of the crystallinity and surface concentration over the activity and benzaldehyde selectivity of the reaction.

## Keywords

*Photo-catalysis; Graphitic carbon nitride; benzyl alcohol; ZnO; Fe<sub>2</sub>O<sub>3</sub>*

## 1. Introduction

As a fundamental field in science, photochemistry development has been improved significantly during the last decades.(Schultz and Yoon, 2011) Advanced oxidation processes and particularly heterogeneous photocatalysis have evolved as powerful technologies to facilitate the control and elimination of pollutants, energy production, as well as selective synthesis of high added value products. (Colmenares et al., 2009; Kubacka et al., 2012; Mamba and Mishra, 2016a) In contrast to studies devoted to photo-degradation of pollutants, relatively fewer studies were conducted on the application of photocatalysis for product synthesis using selective oxidation routes. (Mario J. Muñoz-Batista et al., 2014)

Among the possible alternatives which have a wider electromagnetic spectrum than  $\text{TiO}_2$ , materials with delocalized conjugated  $\pi$  structures have shown a remarkable capacity to transfer electrons under light irradiation. One of these materials, the graphitic carbon nitride (g- $\text{C}_3\text{N}_4$ ), has been extensively studied.(Li et al., 2012; Mamba and Mishra, 2016a; Zhao et al., 2015) Graphitic carbon nitride consists in a graphitic structure of tri-s-triazine layers linked between them through amino groups. It is considered as a promising material as photocatalyst due to its excellent photoelectrical properties, with a band gap suitable for UV-Visible light absorption (2.7 eV). In addition, it can be synthesized using cheap and abundant feedstocks, like melamine,(Fontelles-Carceller et al., 2016; Muñoz-Batista et al., 2017; Yan et al., 2009; Zhang et al., 2013) cyanamide,(Ge et al., 2012) urea,(He et al., 2015b) or thiourea.(Zhang et al., 2012) Pure g- $\text{C}_3\text{N}_4$  shows a good photocatalytic performance under UV, Visible and Sunlight irradiation conditions.(Mamba and Mishra, 2016b) However, it is usually reported that g- $\text{C}_3\text{N}_4$  photo-excited electrons and holes suffer a rapid recombination, resulting in a high decrease of the photoactivity.(Muñoz-Batista et

al., 2015a) The activity of g-C<sub>3</sub>N<sub>4</sub> is related to its surface area, pore volume, physical and chemical surface properties, which makes it versatile and possible to induce different structural modifications to enhance its catalytic properties.(Mamba and Mishra, 2016a) Previous reports showed that is possible to enhance charge separation, improve the resistance to photocorrosion and therefore achieve a higher photocatalytic performance by combining g-C<sub>3</sub>N<sub>4</sub> with another photocatalyst (TiO<sub>2</sub>, ZnO, Fe<sub>2</sub>O<sub>3</sub>). (Evgenidou et al., 2005; He et al., 2015a; Hu et al., 2014; Kuang et al., 2015; Li et al., 2015; Liu et al., 2014; Miranda et al., 2013; M.J. Muñoz-Batista et al., 2014; Muñoz-Batista et al., 2015b; Obregón and Colón, 2014; Theerthagiri et al., 2014; Wang et al., 2017, 2011; Zhou et al., 2015) The most reported method for linking both photocatalysts is wet impregnation, while only a few papers used mechanochemical processes in their synthesis, favoring the use of no solvents. (Kim et al., 2017; Wang et al., 2011) Complete mixture with high interaction level can be achieved without using any other compounds apart from the solid photocatalysts. (Xu et al., 2015)

Benzaldehyde is a highly demanded compound due to its wide variety of applications in food, pharmaceutical or perfumery industry, or as an intermediate in lot of chemical synthesis routes. The commercial benzaldehyde is produced by the chlorination of toluene followed by saponification [39], in which the catalysts offer low selectivity to benzaldehyde and the aldehyde is overoxidized [40].

This work shows the development of ZnO- and Fe<sub>2</sub>O<sub>3</sub>-g-C<sub>3</sub>N<sub>4</sub> using ball milling processes, and their subsequent use in the selective oxidation of benzyl alcohol to benzaldehyde. The complete physico-chemical characterization of the materials attempts to correlate the results with a multitechnique characterization approach using XRD, UV-vis, XPS, SEM-EDX and BET measurements.

## 2. Materials and Methods

### 2.1. Preparation of the samples

The graphitic carbon nitride (CN) was obtained by calcination of melamine (Aldrich), in a semiclosed system (to prevent sublimation) at 550 °C with a heating rate of 5 °C min<sup>-1</sup> during 6 h. The oxide incorporation was subsequently achieved by a simple mechanochemical method in a planetary ball mill under previous reported conditions. (Ouyang et al., 2016) The precursors zinc oxide (Acros Organic) and Iron (III) nitrate (Panreac) for ZnO/g-C<sub>3</sub>N<sub>4</sub> (Zn/CN) and Fe<sub>2</sub>O<sub>3</sub>/g-C<sub>3</sub>N<sub>4</sub> (Fe/CN) were used. For the Fe sample, propionic acid (Andrich) was added before the milling in order to promote the Fe<sub>2</sub>O<sub>3</sub> structure. Finally, the solids were thermally treated at 300 °C for 3h. The sample names were Zn/CN and Fe/CN for the composite samples with 20 and 25 % wt. (elemental data: standard error; 5 %) of ZnO and Fe<sub>2</sub>O<sub>3</sub>, respectively.

### 2.2. Characterization techniques

XRD profiles were obtained with a Bruker D8 DISCOVER A25 diffractometer (Bruker Corporation, Billerica, MA, USA) equipped with a vertical goniometer under theta-theta geometry using Ni filtered Cu K $\alpha$  ( $\lambda = 1.5418 \text{ \AA}$ ) radiation and operated at 40 KeV and 40 mA. Wide angle scanning patterns were collected from 10 ° to 80 ° with a step size of 0.01 ° and counting time of 500 s per step. UV–vis diffuse-reflectance spectroscopy experiments were performed on a spectrophotometer Jasco V-570 (JASCO international Co., Ltd., Hachioji, Tokyo, Japan) equipped with an integrating sphere. The Brunauer–Emmett–Teller (BET) surface areas were determined by N<sub>2</sub> physisorption using a Micromeritics ASAP 2020 automated system (Micromeritics Instrument Corporation, Norcross, GA, USA). Prior to adsorption measurements, samples were

degassed under vacuum (0.1 Pa) for 4 h at 130 °C. Scanning electron microscopy images were recorded with a JEOL JSM-6300 scanning microscope (JEOL Ltd., Akishima, Tokyo, Japan) equipped with Energy-dispersive X-ray spectroscopy (EDX) at 20 kV. An Au/Pd coating was employed to analyze samples on a high-resolution sputtering SC7640 instrument (Quorum Technologies Ltd., Lewes, England, UK) (up to 7 nm thickness) at a sputtering rate of 1.5 kV per minute. XPS data were recorded using a VG Scientific photoelectron spectrometer ESCALAB-210 (Thermo Scientific, Waltham, MA, USA) with Al K $\alpha$  radiation (1486.6 eV) from an X-ray source, operating at 15 kV and 20 mA. Survey spectra in the energy range from 0 to 1350 eV with 0.4 eV step were recorded for all the samples. High resolution spectra were recorded with 0.1 eV step, 100 ms dwell time and 25 eV pass energy. Curve fitting was carried out using the CasaXPS software (Casa Software Ltd., Cheshire, England, UK) using C 1s as energy reference (284.6 eV). Surface chemical contributions were estimated from XP-spectra, by calculating the integral of each peak after subtraction of the “S-shaped” Shirley-type background using the appropriate experimental sensitivity factors.

### *2.3. Photo-catalytic experiments*

Photooxidation of benzyl alcohol experiments were carried out in a Pyrex cylindrical double-wall immersion well reactor equipped with medium pressure 125 W mercury lamp ( $\lambda = 365$  nm), which was supplied by Photochemical Reactors Ltd. UK (Model RQ 3010), (Reading, UK). The distance between the light source and reaction media was ca. 10 mm and irradiance of the light source reached 1845.6 W/m<sup>2</sup>. Magnetic stirring with a speed of 1100 rpm was used in the batch reactor to obtain an homogenous suspension of the photocatalysts. Reaction temperature was fixed at 30 °C. A solution of 1.5 mM benzyl alcohol (Sigma-Aldrich Inc., St. Louis, MO, USA) was

prepared in acetonitrile (Sigma-Aldrich Inc., St. Louis, MO, USA) medium. Experiments were carried out using 150 mL of the mother solution and 1 g/L of catalyst concentration for 4 h under UV light and air bubbling conditions (25 mL/min). In order to equilibrate the adsorption-desorption over the photocatalyst surface, the reaction solution was left in the dark for 30 min before each reaction.

Samples were periodically taken (ca. 1 mL) from the photoreactor at different times and filtered off (0.20 µm, 25 µm, nylon filters). The concentration of model compound was determined by a high performance liquid chromatography (HPLC, Waters Model 590 pump) (Waters Limited, Hertfordshire, UK) equipped with a dual absorbance detector (Waters 2487) and the SunFire™ C18 (3.5 µm, 150 mm length, 4.6 mm inner diameter) column provided by Waters. The mobile phase was Milli-Q water/acetonitrile/methanol in the volumetric ratio of 77.5:20:2.5 with 0.1% of H<sub>3</sub>PO<sub>4</sub> (Sigma-Aldrich Inc., St. Louis, MO, USA). We used isocratic elution at a flow rate of 1 mL/min. The injection volume was 10 µL. TiO<sub>2</sub> P25 (Evonik Industries AG, Essen, Germany) were used as reference. Carbon balance above 96% was obtained in all experiments.

### **3. Results and Discussion**

#### *3.1. Characterization results*

Figure 1 shows the XRD spectra of the two samples studied and the CN reference. The characteristic structure of the CN nanomaterial can be observed. It showed two peaks (13.25 and 27 degrees). The most intense peak is commonly associated to the interlayer-stacking structure (002). On the other hand, the other minor peak is attributed to (100) interlayer reflection. (Fontelles-Carceller et al., 2016) The composite samples showed significant differences related to the degree of crystallinity. The Zn/CN composite sample showed a very crystallized structure with sharp peaks that can be associated with

the ZnO compound. In addition to the peaks related to the CN structure, the existence of the zincite ZnO phase (JCPDS 36-1451) was detected.(Boyle et al., 2002) On the other hand, it was observed that iron component show an structure dominated for an amorphous phase.

According to the summarized data presented in Table 1, the CN reference showed a relatively low surface area value ( $10 \text{ m}^2 \text{ g}^{-1}$ ). This value was not modified when the ZnO component was introduced in the structure. Besides, a marked increase with respect to the active CN support was observed for the Fe/CN sample.

The optical properties of the samples were analyzed with UV–vis spectroscopy. Figure 2 shows the spectra for the two composite samples and the CN reference. The CN showed a band gap energy of 2.7 eV, in accordance with literature reports.(Mamba and Mishra, 2016a) Figure 2 shows that the spectra of Zn/CN sample presented a very similar profile to the pure CN reference. According to this information, it can be considered that the optical properties of the composite material Zn/CN were defined by the CN component (sharp absorption edge at 450 nm), leading to similar band gap values, which were reported in the second column of Table 1. In addition, the existence of the strong absorption edge near 575 nm for the Fe/CN and Band Gap of 1.3 eV were attributed to the band-gap energy absorption of the Fe component in the structure.

The structure of the samples was also studied using XPS. Figure 3 presents the results for carbon C1s (A) and nitrogen N1s (B) regions for the two composite samples, as well as the zinc Zn 2p (C) and iron Fe 2p (D) regions for the Zn/CN and Fe/CN samples, respectively. For the C 1s (Figure 3A), the contributions associated with the C-C bond (284.6 eV), C<sub>3</sub>-N (286.2 eV) and N-C-N (288.0 eV) were detected.(Dong et al., 2014; Miranda et al., 2013; Muñoz-Batista et al., 2015a) All contributions, were associated with the CN structure. In addition, the latter two were also detected in the N 1s region

(Figure 3B). C<sub>3</sub>-N (399.6 eV) and N-C-N (398. eV). Additionally, in this region the component N-H at 400.9 eV and the typical contribution of CN Pi-exc at 404.5 eV were detected. (Dong et al., 2014; Miranda et al., 2013; Muñoz-Batista et al., 2015a) No significant differences were observed between the two composite samples concerning the structure of the CN. Both the energy and the distances between the contributions remained essentially constant, indicating that the CN structure was stable during the synthesis process. The XPS study also gave information about the Zn and Fe components. The energy values for the Zn 2p (1021.5 eV) and Fe 2p (710.6 eV) regions confirmed the presence of ZnO and Fe<sub>2</sub>O<sub>3</sub> in the Zn/CN and Fe/CN samples, respectively.(Wanger et al., 1979) Finally, a very low surface concentration of the oxide component for the Zn/CN sample was observed in Figure 3 (C and D), although both had a similar ZnO or Fe<sub>2</sub>O<sub>3</sub> content.

The characterization of the samples was completed using SEM. Figure 4A (Zn/CN sample) shows a highly crystallized particle, a big crystallized structure corresponding to CN, recovered of some crystals corresponding to ZnO particles. The information enclosed in the mapping indicates that a significant part of ZnO was heterogeneously distributed in the CN structure (Figure 4B). On the other hand, the Fe/CN image (Figure 4B) showed a particle which according to the EDX-mapping analysis (Figure 4D), was covered with smaller particles of Fe<sub>2</sub>O<sub>3</sub>.

### *3.2. Catalytic results*

Figure 5 shows the conversion and selectivity to benzaldehyde results of CN reference and composite samples. Figure 5 also includes the conversion and selectivity observable when P25 commercial catalyst was tested. The CN reference showed no activity during the oxidation of benzyl alcohol. Focusing on the synthesized composite samples, it can

be observed that the structure modification of the CN with ZnO and Fe<sub>2</sub>O<sub>3</sub> caused an increase in the activity. particularly, this increase was marked for the Fe/CN sample. The maximum conversion was obtained for the Fe/CN (20 %), presenting an enhancement ratio with respect to the Zn/CN of 2. Amorphous structures have usually displayed low activity, which was attributed to low carrier mobilities, resulting in inefficient photocatalysis.(Kakuta and Abe, 2009) However, previous studies reported that amorphous TiO<sub>2</sub> or Fe<sub>2</sub>O<sub>3</sub> showed very similar activity compared to the fully crystallized phase. (Augugliaro et al., 2008; Kakuta and Abe, 2009; Li et al., 2007) Figure 5 shows that both Zn/CN and Fe/CN samples led to an enhancement of the selectivity to partial oxidation product of benzyl alcohol. The other reaction product (not shown in the Figure 5) corresponded to the complete mineralization of the alcohol (CO<sub>2</sub>). The production of the total oxidation product requires a significantly larger number of charge carriers and energetic photons,(Bertolini et al., 2018) which are likely less available in the amorphous Fe/CN composite sample. This could partially explain the selectivity data; 70% benzaldehyde selectivity for Fe/CN sample. Beside the crystallinity factor, the composite samples showed significant differences concerning the oxide surface concentration obtained by XPS. Figure 6 shows the conversion and selectivity to benzaldehyde as function of the fraction  $M/(C + N)$  with the aim of visualizing these differences. M represents the concentration of the metallic component (Zn or Fe). The conversion and selectivity data, as well as the fraction obtained, were normalized to ease the visualization of the differences between samples. Figure 6 showed very strong correlation in the behavior of the conversion and selectivity. The Zn/CN sample presented an extremely low surface concentration of ZnO, which together with the heterogeneity of high crystallized structure (detected by SEM-EDX mapping and XRD studies) caused a relatively low activity and selectivity. On the other

hand, a high surface concentration of the homogeneously distributed amorphous Fe component resulted in an enhancement of the conversion and selectivity to benzaldehyde. The similar trends showed in Figure 6 indicated that maximum activity and benzaldehyde selectivity could be associated also with the maximum surface concentration of the metal compound. This enhancement of the benzaldehyde selectivity was achieved by maintaining a relatively high level of activity compared with the P25 commercial photocatalyst which generally shows good results for a large number of reactions.

#### **4. Conclusions**

Binary composite samples of ZnO or Fe<sub>2</sub>O<sub>3</sub> in contact with the organic semiconductor g-C<sub>3</sub>N<sub>4</sub> were synthesized using a simple one-pot mechanochemical method. The inclusion of oxides phases led to semiconductors with catalytic activity during the oxidation of benzyl alcohol. The obtained results suggested that different parameters affected the activity and benzaldehyde selectivity. The best activity and selectivity results were obtained for the composite system with g-C<sub>3</sub>N<sub>4</sub> and the amorphous Fe<sub>2</sub>O<sub>3</sub> component. The amorphous structure could be modifying the charge handling of g-C<sub>3</sub>N<sub>4</sub>, limiting the CO<sub>2</sub> photo-production due to the complete mineralization of the alcohol. On the other hand, SEM and XPS clearly indicated that the enhancement of the activity and selectivity to benzaldehyde was associated with the concentration of the metal component on the surface, as well as with the homogeneity in the structure.

## 5. Acknowledgments

Rafael Luque funding from the European Union's Horizon 2020 research and innovation programme under the Marie Skłodowska-Curie grant agreement No 641861 (for funding Weyi Ouyang Ph.D studies). Mario Munoz-Batista gratefully acknowledges MINECO for a JdC contract (Ref. FJCI-2016-29014).

## References

- Augugliaro, V., Caronna, T., Loddo, V., Marci, G., Palmisano, G., Palmisano, L., Yurdakal, S., 2008. Oxidation of aromatic alcohols in irradiated aqueous suspensions of commercial and home-prepared rutile TiO<sub>2</sub>: A selectivity study. *Chem. - A Eur. J.* 14, 4640–4646. <https://doi.org/10.1002/chem.200702044>
- Bertolini, G.R., Pizzio, L.R., Kubacka, A., Muñoz-Batista, M.J., Fernández-García, M., 2018. Composite H<sub>3</sub>PW<sub>12</sub>O<sub>40</sub>-TiO<sub>2</sub> catalysts for toluene selective photo-oxidation. *Appl. Catal. B Environ.* 225. <https://doi.org/10.1016/j.apcatb.2017.11.055>
- Boyle, D.S., Govender, K., O'Brien, P., 2002. Novel low temperature solution deposition of perpendicularly orientated rods of ZnO: substrate effects and evidence of the importance of counter-ions in the control of crystallite growth. *Chem. Commun.* 0, 80–81. <https://doi.org/10.1039/b110079n>
- Colmenares, J.C., Luque, R., Campelo, J.M., Colmenares, F., Karpiński, Z., Romero, A.A., 2009. Nanostructured Photocatalysts and Their Applications in the Photocatalytic Transformation of Lignocellulosic Biomass: An Overview. *Materials (Basel)*. 2, 2228–2258. <https://doi.org/10.3390/ma2042228>
- Dong, G., Zhang, Y., Pan, Q., Qiu, J., 2014. A fantastic graphitic carbon nitride (g-

- C3N4) material: Electronic structure, photocatalytic and photoelectronic properties. *J. Photochem. Photobiol. C Photochem. Rev.* 20, 33–50.  
<https://doi.org/10.1016/j.jphotochemrev.2014.04.002>
- Evgenidou, E., Fytianos, K., Poullos, I., 2005. Semiconductor-sensitized photodegradation of dichlorvos in water using TiO<sub>2</sub> and ZnO as catalysts. *Appl. Catal. B Environ.* 59, 81–89. <https://doi.org/10.1016/J.APCATB.2005.01.005>
- Fontelles-Carceller, O., Muñoz-Batista, M.J., Fernández-García, M., Kubacka, A., 2016. Interface Effects in Sunlight-Driven Ag/g-C<sub>3</sub>N<sub>4</sub> Composite Catalysts: Study of the Toluene Photodegradation Quantum Efficiency. *ACS Appl. Mater. Interfaces* 8. <https://doi.org/10.1021/acsami.5b10434>
- Ge, L., Zuo, F., Liu, J., Ma, Q., Wang, C., Sun, D., Bartels, L., Feng, P., 2012. Synthesis and Efficient Visible Light Photocatalytic Hydrogen Evolution of Polymeric g-C<sub>3</sub>N<sub>4</sub> Coupled with CdS Quantum Dots. *J. Phys. Chem. C* 116, 13708–13714. <https://doi.org/10.1021/jp3041692>
- He, Y., Wang, Y., Zhang, L., Teng, B., Fan, M., 2015a. High-efficiency conversion of CO<sub>2</sub> to fuel over ZnO/g-C<sub>3</sub>N<sub>4</sub> photocatalyst. *Appl. Catal. B Environ.* 168–169, 1–8. <https://doi.org/10.1016/J.APCATB.2014.12.017>
- He, Y., Zhang, L., Teng, B., Fan, M., 2015b. New Application of Z-Scheme Ag<sub>3</sub>PO<sub>4</sub>/g-C<sub>3</sub>N<sub>4</sub> Composite in Converting CO<sub>2</sub> to Fuel. *Environ. Sci. Technol.* 49, 649–656. <https://doi.org/10.1021/es5046309>
- Hu, S., Jin, R., Lu, G., Liu, D., Gui, J., 2014. The properties and photocatalytic performance comparison of Fe<sup>3+</sup>-doped g-C<sub>3</sub>N<sub>4</sub> and Fe<sub>2</sub>O<sub>3</sub>/g-C<sub>3</sub>N<sub>4</sub> composite catalysts. *RSC Adv.* 4, 24863. <https://doi.org/10.1039/c4ra03290j>
- Kakuta, S., Abe, T., 2009. Photocatalysis for water oxidation by Fe<sub>2</sub>O<sub>3</sub> nanoparticles

embedded in clay compound: Correlation between its polymorphs and their photocatalytic activities. *J. Mater. Sci.* 44, 2890–2898.

<https://doi.org/10.1007/s10853-009-3382-2>

Kim, J.S., Oh, J.W., Woo, S.I., 2017. Investigation for the effects of ball milling process on the physical characteristics, the behaviors of carriers and the photocatalytic activity of sulfur doped g-C<sub>3</sub>N<sub>4</sub>. *Int. J. Hydrogen Energy* 42, 5485–5495.

<https://doi.org/10.1016/J.IJHYDENE.2016.08.077>

Kuang, P.-Y., Su, Y.-Z., Chen, G.-F., Luo, Z., Xing, S.-Y., Li, N., Liu, Z.-Q., 2015. g-C<sub>3</sub>N<sub>4</sub> decorated ZnO nanorod arrays for enhanced photoelectrocatalytic performance. *Appl. Surf. Sci.* 358, 296–303.

<https://doi.org/10.1016/J.APSUSC.2015.08.066>

Kubacka, A., Fernández-García, M., Colón, G., 2012. Advanced nanoarchitectures for solar photocatalytic applications. *Chem. Rev.* 112, 1555–614.

<https://doi.org/10.1021/cr100454n>

Li, K., Gao, S., Wang, Q., Xu, H., Wang, Z., Huang, B., Dai, Y., Lu, J., 2015. In-Situ-Reduced Synthesis of Ti<sup>3+</sup> Self-Doped TiO<sub>2</sub>/g-C<sub>3</sub>N<sub>4</sub> Heterojunctions with High Photocatalytic Performance under LED Light Irradiation. *ACS Appl. Mater. Interfaces* 7, 9023–9030. <https://doi.org/10.1021/am508505n>

Li, L., Chu, Y., Liu, Y., Dong, L., 2007. Template-Free Synthesis and Photocatalytic Properties of Novel Fe<sub>2</sub>O<sub>3</sub> Hollow Spheres. *J. Phys. Chem. C* 111, 2123–2127.

<https://doi.org/10.1021/jp066664y>

Li, X.-H., Wang, X., Antonietti, M., 2012. Solvent-Free and Metal-Free Oxidation of Toluene Using O<sub>2</sub> and g-C<sub>3</sub>N<sub>4</sub> with Nanopores: Nanostructure Boosts the Catalytic Selectivity. *ACS Catal.* 2, 2082–2086. <https://doi.org/10.1021/cs300413x>

- Liu, Y., Yu, Y.-X., Zhang, W.-D., 2014. Photoelectrochemical study on charge transfer properties of nanostructured Fe<sub>2</sub>O<sub>3</sub> modified by g-C<sub>3</sub>N<sub>4</sub>. *Int. J. Hydrogen Energy* 39, 9105–9113. <https://doi.org/10.1016/J.IJHYDENE.2014.03.248>
- Mamba, G., Mishra, A.K., 2016a. Graphitic carbon nitride (g-C<sub>3</sub>N<sub>4</sub>) nanocomposites: A new and exciting generation of visible light driven photocatalysts for environmental pollution remediation. *Appl. Catal. B Environ.* 198, 347–377. <https://doi.org/10.1016/j.apcatb.2016.05.052>
- Mamba, G., Mishra, A.K., 2016b. Graphitic carbon nitride (g-C<sub>3</sub>N<sub>4</sub>) nanocomposites: A new and exciting generation of visible light driven photocatalysts for environmental pollution remediation. *Appl. Catal. B Environ.* 198, 347–377. <https://doi.org/10.1016/J.APCATB.2016.05.052>
- Miranda, C., Mansilla, H., Yáñez, J., Obregón, S., Colón, G., 2013. Improved photocatalytic activity of g-C<sub>3</sub>N<sub>4</sub>/TiO<sub>2</sub> composites prepared by a simple impregnation method. *J. Photochem. Photobiol. A Chem.* 253, 16–21. <https://doi.org/10.1016/j.jphotochem.2012.12.014>
- Muñoz-Batista, M.J., Fernández-García, M., Kubacka, A., 2015a. Promotion of CeO<sub>2</sub>–TiO<sub>2</sub> photoactivity by g-C<sub>3</sub>N<sub>4</sub>: Ultraviolet and visible light elimination of toluene. *Appl. Catal. B Environ.* 164, 261–270. <https://doi.org/10.1016/j.apcatb.2014.09.037>
- Muñoz-Batista, M.J., Fontelles-Carceller, O., Kubacka, A., Fernández-García, M., 2017. Effect of exfoliation and surface deposition of MnO<sub>x</sub> species in g-C<sub>3</sub>N<sub>4</sub>: Toluene photo-degradation under UV and visible light. *Appl. Catal. B Environ.* 203, 663–672. <https://doi.org/10.1016/j.apcatb.2016.10.044>
- Muñoz-Batista, M.J., Kubacka, A., Fernández-García, M., 2014. Effect of g-C<sub>3</sub>N<sub>4</sub>

loading on TiO<sub>2</sub>-based photocatalysts: UV and visible degradation of toluene.  
Catal. Sci. Technol. 4, 2006. <https://doi.org/10.1039/c4cy00226a>

Muñoz-Batista, M.J., Kubacka, A., Rachwalik, R., Bachiller-Baeza, B., Fernández-García, M., 2014. Green photo-oxidation of styrene over W–Ti composite catalysts. J. Catal. 309, 428–438. <https://doi.org/10.1016/j.jcat.2013.10.021>

Muñoz-Batista, M.J., Nasalevich, M.A., Savenije, T.J., Kapteijn, F., Gascon, J., Kubacka, A., Fernández-García, M., 2015b. Enhancing promoting effects in g-C<sub>3</sub>N<sub>4</sub>-Mn<sup>+</sup>/CeO<sub>2</sub>-TiO<sub>2</sub> ternary composites: Photo-handling of charge carriers. Appl. Catal. B Environ. 176–177, 687–698. <https://doi.org/10.1016/j.apcatb.2015.04.051>

Obregón, S., Colón, G., 2014. Improved H<sub>2</sub> production of Pt-TiO<sub>2</sub>/g-C<sub>3</sub>N<sub>4</sub>-MnOx composites by an efficient handling of photogenerated charge pairs. Appl. Catal. B Environ. 144, 775–782. <https://doi.org/10.1016/j.apcatb.2013.07.034>

Ouyang, W., Kuna, E., Yepez, A., Balu, A., Romero, A., Colmenares, J., Luque, R., 2016. Mechanochemical Synthesis of TiO<sub>2</sub> Nanocomposites as Photocatalysts for Benzyl Alcohol Photo-Oxidation. Nanomaterials 6, 93. <https://doi.org/10.3390/nano6050093>

Schultz, D.M., Yoon, T.P., 2011. Solar Synthesis: Prospects in Visible Light Photocatalysis. Science (80-. ). 334, 1114–1117. <https://doi.org/10.1126/science.1213920>

Theerthagiri, J., Senthil, R.A., Priya, A., Madhavan, J., Michael, R.J. V., Ashokkumar, M., 2014. Photocatalytic and photoelectrochemical studies of visible-light active  $\alpha$ -Fe<sub>2</sub>O<sub>3</sub>-g-C<sub>3</sub>N<sub>4</sub> nanocomposites. RSC Adv. 4, 38222–38229. <https://doi.org/10.1039/C4RA04266B>

- Wang, W., Liu, Y., Qu, J., Chen, Y., Tadé, M.O., Shao, Z., 2017. Synthesis of Hierarchical TiO<sub>2</sub>-C<sub>3</sub>N<sub>4</sub> Hybrid Microspheres with Enhanced Photocatalytic and Photovoltaic Activities by Maximizing the Synergistic Effect. *ChemPhotoChem* 1, 35–45. <https://doi.org/10.1002/cptc.201600021>
- Wang, Y., Shi, R., Lin, J., Zhu, Y., 2011. Enhancement of photocurrent and photocatalytic activity of ZnO hybridized with graphite-like C<sub>3</sub>N<sub>4</sub>. *Energy Environ. Sci.* 4, 2922. <https://doi.org/10.1039/c0ee00825g>
- Wanger, C.D., Riggs, W.M., Davis, L.E., Moulder, J.F., E.Muilenberg, G., 1979. Handbook of x-ray photoelectron spectroscopy: a reference book of standard data for use in x-ray photoelectron spectroscopy. Physical Electronics Division, Perkin-Elmer Corp.
- Xu, C., De, S., Balu, A.M., Ojeda, M., Luque, R., 2015. Mechanochemical synthesis of advanced nanomaterials for catalytic applications. *Chem. Commun.* 51, 6698–6713. <https://doi.org/10.1039/C4CC09876E>
- Yan, S.C., Li, Z.S., Zou, Z.G., 2009. Photodegradation Performance of g-C<sub>3</sub>N<sub>4</sub> Fabricated by Directly Heating Melamine. *Langmuir* 25, 10397–10401. <https://doi.org/10.1021/la900923z>
- Zhang, G., Zhang, J., Zhang, M., Wang, X., 2012. Polycondensation of thiourea into carbon nitride semiconductors as visible light photocatalysts. *J. Mater. Chem.* 22, 8083. <https://doi.org/10.1039/c2jm00097k>
- Zhang, Y., Pan, Q., Chai, G., Liang, M., Dong, G., Zhang, Q., Qiu, J., 2013. Synthesis and luminescence mechanism of multicolor-emitting g-C<sub>3</sub>N<sub>4</sub> nanopowders by low temperature thermal condensation of melamine. *Sci. Rep.* 3. <https://doi.org/10.1038/srep01943>

Zhao, Z., Sun, Y., Dong, F., 2015. Graphitic carbon nitride based nanocomposites: a review. *Nanoscale* 7, 15–37. <https://doi.org/10.1039/c4nr03008g>

Zhou, J., Zhang, M., Zhu, Y., 2015. Photocatalytic enhancement of hybrid C<sub>3</sub>N<sub>4</sub>/TiO<sub>2</sub> prepared via ball milling method. *Phys. Chem. Chem. Phys.* 17, 3647–3652. <https://doi.org/10.1039/C4CP05173D>

## Tables

**Table 1.** BET surface area and Band Gap of the samples.<sup>a</sup>

Sample	BET surface area (m <sup>2</sup> /g)	Band Gap (eV)
CN	10	2.7
Zn/CN	10	2.7
Fe/CN	27	1.3

<sup>a</sup>Standard error. BET surface area: 1.5 m<sup>2</sup>/g. Band Gap: 0.05 eV

## Figure Captions

**Figure 1.** XRD spectra of CN, Zn/CN and Fe/CN samples.

**Figure 2.** UV-vis spectra of CN, Zn/CN and Fe/CN samples.

**Figure 3.** (A) C 1s, (B) Ni 1s, (C) Zn 2p and (D) Fe 2p XPS spectra of the samples.

**Figure 4.** SEM images and mapping analysis: (A) and (B) Zn/CN sample. (C) and (D) Fe/CN sample.

**Figure 5.** Conversion and Benzaldehyde selectivity of the samples and references.

**Figure 6.** Conversion and benzaldehyde (Bz) selectivity as a function of the Metal (M) fraction detected by XPS.

## Figures

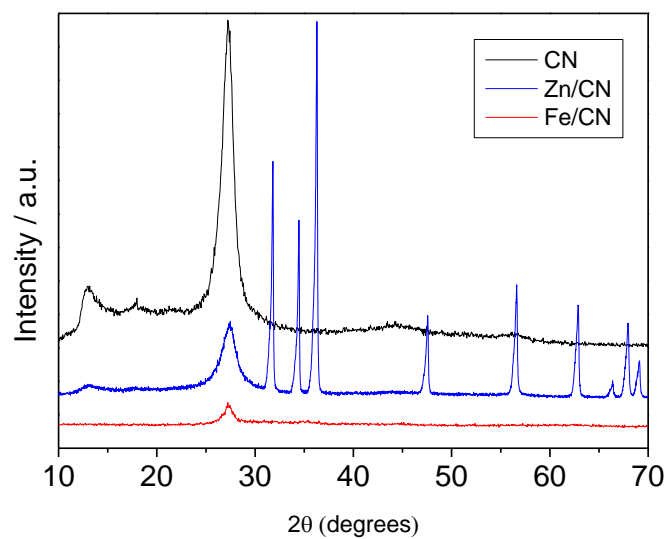


**Figure 1.** XRD spectra of CN, Zn/CN and Fe/CN samples.

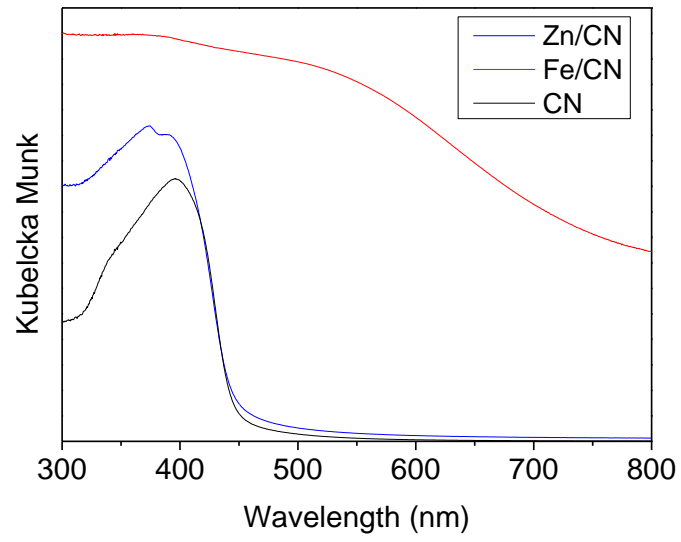


**Figure 2.** UV-vis spectra of CN, Zn/CN and Fe/CN samples.

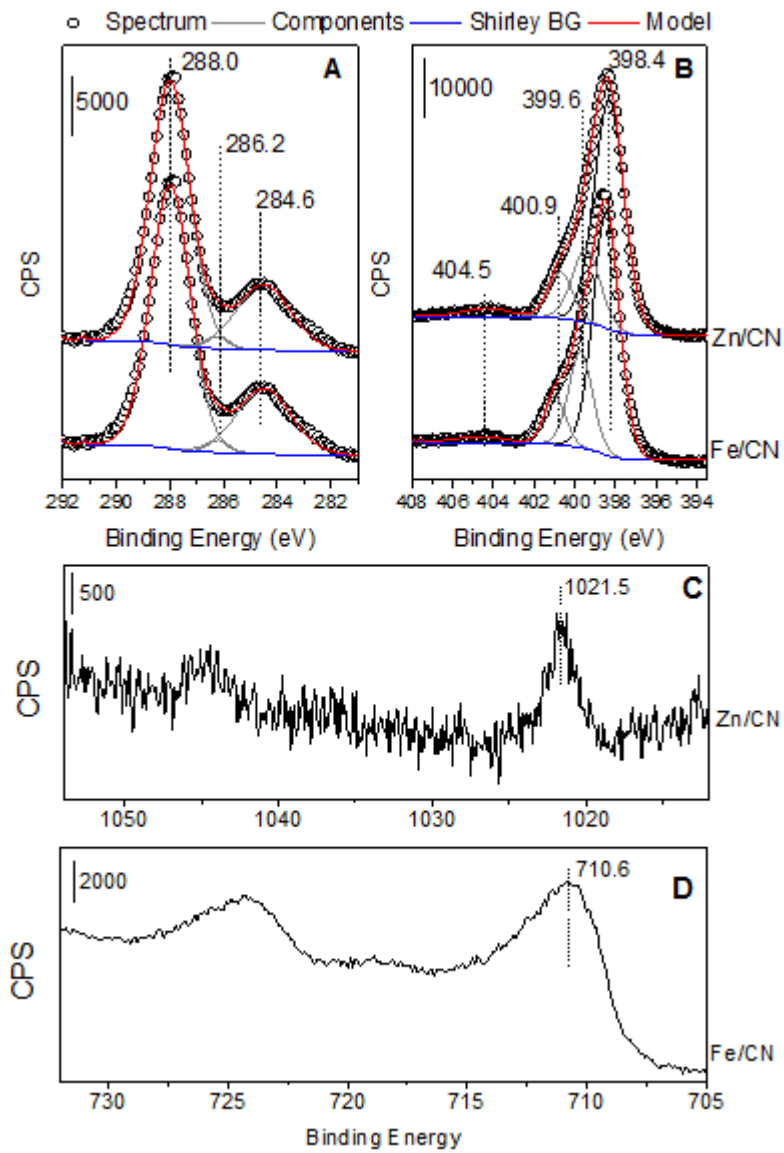


**Figure 3.** (A) C 1s, (B) Ni 1s, (C) Zn 2p and (D) Fe 2p XPS spectra of the samples.

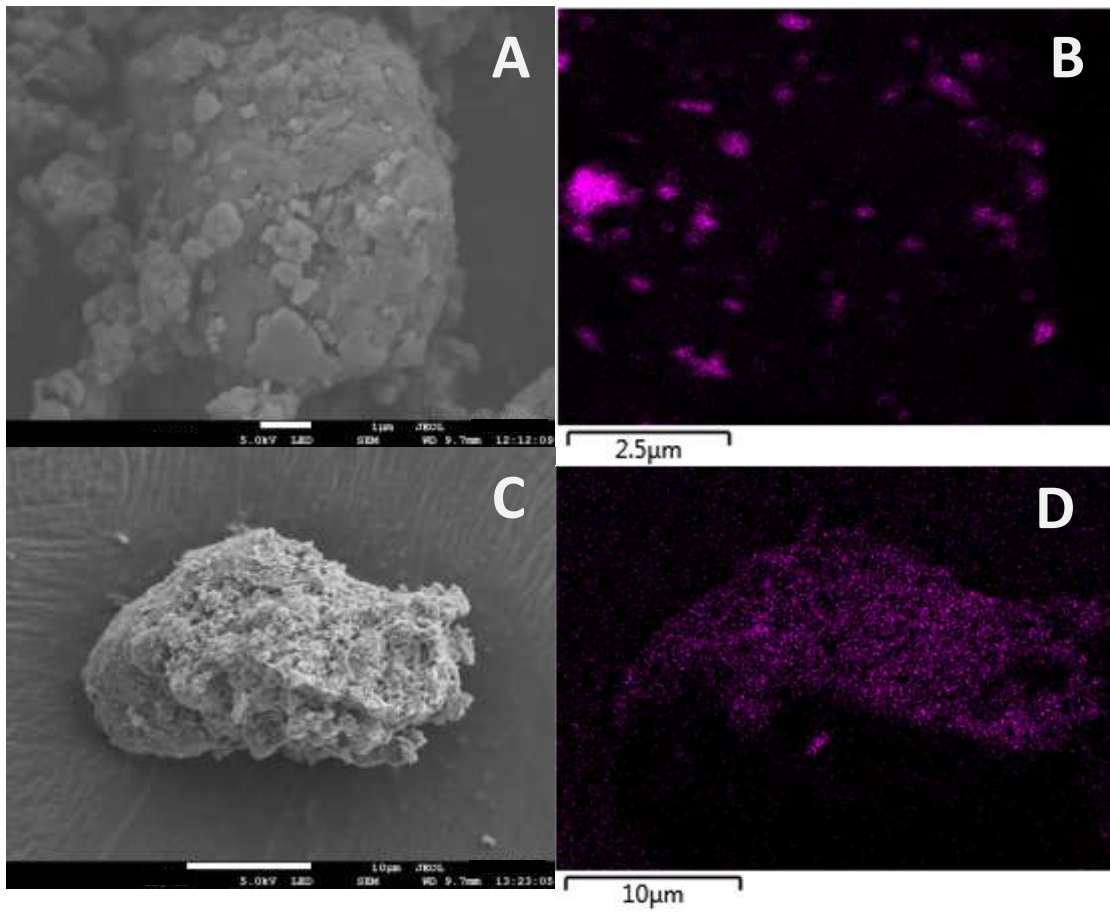


**Figure 4.** SEM images and mapping analysis: (A) and (B) Zn/CN sample. (C) and (D) Fe/CN sample.

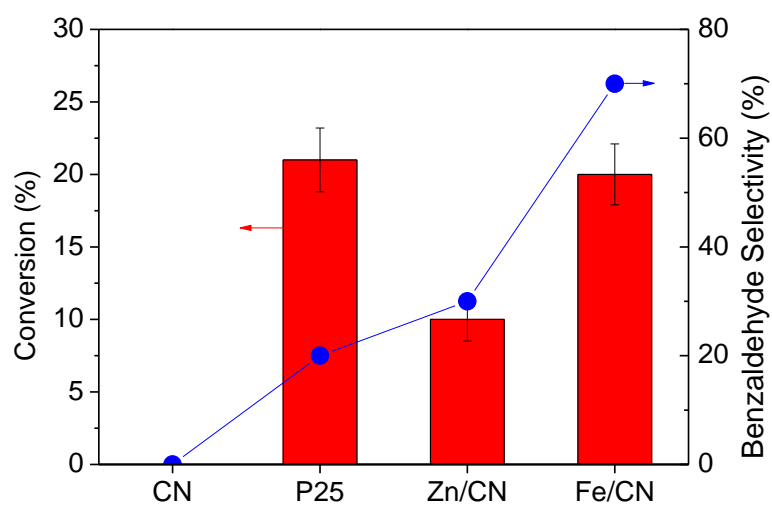


**Figure 5.** Conversion and Benzaldehyde selectivity of the samples and references.

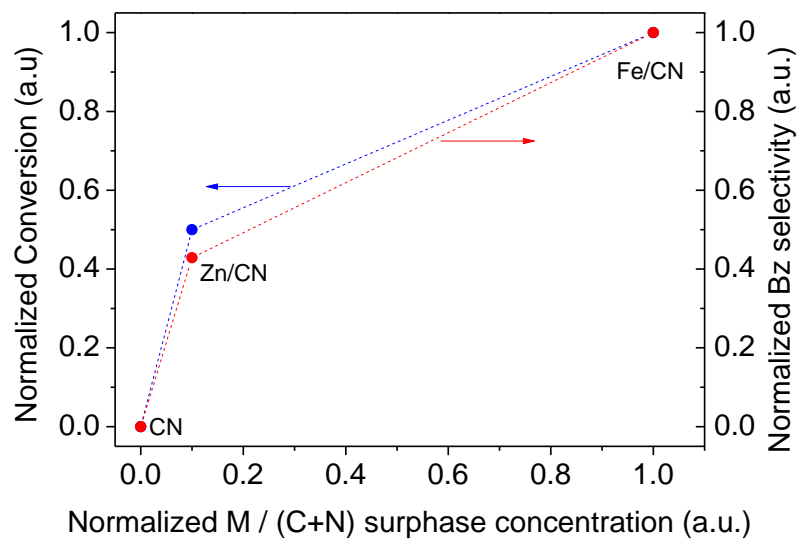


**Figure 6.** Conversion and benzaldehyde (Bz) selectivity as a function of the Metal (M) fraction detected by XPS.